ORIGINAL ARTICLE

Finishing mechanism modelling on magnetic abrasive finishing behaviours with core-shell magnetic abrasive particles

Xinjian Zhang[1] · Xudong Zhao[1] · Bo Cheng[1] · Yu Wang[1] · Qiang Song[2] · Chunzhi Zhang[2] · Wensheng Li[1,2] · Uladzimir Seniuts[3] · Marat Belotsrkovsky[3] · Zhornik Viktor[3]

Abstract

Efficiency and precision are two key indicators in the magnetic abrasive finishing (MAF) process. This paper presents the design of a core-shell structured magnetic abrasive particles (MAPs) with enhanced magnetic saturation rate and improved morphology. In addition, a processing roughness model based on indentation theory was developed by determining the number of active abrasive particles within the MAPs. The evolution of the MAF mechanism during the elastic and plastic deformation of processing material is clarified to realise high MAF efficiency and precision on slender tube surfaces. The grooves that slot on magnetic poles drive the maximum magnetic force on the MAPs. The simulation results from both the theoretical model of magnetic force and the active abrasive particle number theory are consistent with the actual experimental parameters, which effectively predict and explain the MAF phenomenon and mechanism. As to the zirconium alloy tube, the maximum improvement of five MAF passes on surface roughness *Ra* using the designed MAP is 63.38%, with the roughness *Ra* reaching 0.119 μm.

Keywords Magnetic · Models · Magnetic abrasive finishing · Magnetic abrasives · Indentation · Surface · Abrasive · Roughness

1 Introduction

As the reliability and durability of equipment parts rely on their surface integrity, the presence of a rough surface on the workpiece can result in uneven growth of oxide film during the oxidation process under extreme conditions, such as high temperature and high pressure, in industries like nuclear cladding tubes and aircraft oil pipelines. This uneven growth leads to localised stress, gradual formation of micro-cracks and even potential industrial safety accidents

✉ Wensheng Li
liws@lut.edu.cn

1   State Key Laboratory of Advanced Processing and Recycling of Non-ferrous Metal, School of Materials Science and Engineering, Lanzhou University of Technology, Lanzhou 730050, Gansu, China

2   School of Materials Science and Engineering, Shandong University of Science and Technology, Qingdao 266590, Shandong, China

3   The Joint Institute of Mechanical Engineering, National Academy of Sciences of Belarus, 220072 Minsk, Belarus

[1]. Conventional machining methods, such as grinding and honing, involving the use of rigid tools, exacerbate the formation of micro-cracks and residual tensile stress on the surface. To address these issues, a novel finishing method known as magnetic abrasive finishing (MAF) has been developed. MAF utilises magnetic fields to drive magnetic abrasive particles (MAPs) for processing, effectively reducing surface roughness and enhancing mechanical properties. Notably, MAF demonstrates significant potential for improving the surface quality of elongated structural tubes in various industries, including nuclear, aeronautical, medical and others.

MAF has been employed for processing the inner and outer surfaces of tubular parts and flat parts. Shinmura et al. studied the processing of Si3N4 fine ceramic bars with a diameter of 12 mm, and investigated the effect of MAP size on the removal and surface finishing of cylindrical finishing [2]. Yamaguchi et al. elucidated the machining principle and equipment of MAF in capillaries, supporting the application of this method to extra-long tubes [3, 4]. Wang et al. developed a MAF system that effectively polished a large number of freeform surface assemblies,

verifying the feasibility of MAF process [5]. To improve the efficiency of the MAF process, some researchers optimised the distribution of magnetic field, and combined MAF with other processes, such as the addition of ultrasonic vibration on the workpiece, which focused on the impact of the MAF process on the surface integrity and uniformity of workpiece. Zhou et al. proposed an ultrasonic vibration-assisted magnetic abrasive finishing for surface treatment. The finishing experiments demonstrated that the efficiency of ultrasonic abrasives was 40% higher than that of magnetic abrasives finishing [6]. Kwak proposed a practical method that mounted a permanent magnet on the other side of the machined workpiece to improve the magnetic field intensity of the magnesium sheet [7]. In order to further improve the processing quality, recent researches focus on processing efficiency and precision control through the investigation of the elimination mechanism [8–10]. Jain et al. developed an empirical model for force prediction, and analysed the influence of process parameters on normal force and tangential force during ferromagnetic and non-ferromagnetic flat materials polishing [11, 12]. In addition, they established a surface roughness model for flat workpieces and considered the surface profile distribution before MAF as Gaussian distribution based on the empirical model, thus deepening the understanding of the material removal mechanism in MAF process [13, 14]. Misra et al. developed a mathematical model of surface roughness in the ultrasonic-assisted magnetic abrasive finishing (UAMAF) process and experimentally verified the model's reliability on a stainless steel flat workpiece [15]. The model confirmed that a critical surface roughness value could be obtained from the given machining parameter, below which the roughness value stopped decreasing. Zhao et al. modelled the normal pressure of the MAP prepared by the atomisation method and revealed that the diamond MAP exerted a better processing effect on SS304 plane material than the CBN MAP and the alumina MAP under the same optimal process conditions [16].

In contrast to previous roughness models developed for flat workpieces composed of various materials, this research presents a novel roughness model specifically tailored for a slender zirconium alloy tube. The study focuses on enhancing the uniformity and gradient of the magnetic field distribution along the outer wall of the tube by altering the configuration of the magnetic poles. Furthermore, MAP is the critical factor to determine processing efficiency and precision. There are problems such as uneven MAP particle size and unreasonable distribution of hard particles, which lead to unstable processing effects. This paper proposes the number theory of active abrasive particles by designing and preparing the core-shell type Fe-SiC MAPs, and a corresponding theoretical model of the MAF force acting on MAPs by selecting zirconium alloy tube, which clarifies

the evolution of MAF mechanism on tubular workpieces. The roughness model is established based on the indentation amount of active abrasive particles. Given the potential of MAPs and the process, zirconium alloy tubes are adopted as subjects to explore the finishing effect of this process.

2 Experimental and theoretical modes

2.1 MAF experiment implementation and schematic diagram

Figure 1 depicts the experimental MAF equipment built by modifying the original connection between the tool and the spindle chuck of a real lathe. Two Nd–Fe–B magnetic poles of the N pole and the S pole are fixed on the disc to form a magnetic field generation device. The shapes of poles are optimised through finite element method to simulate the change of magnetic flux and to explore the role of their shapes on the MAF effect. The MAPs prepared by a two-step mechanical sintering method are adsorbed on magnetic poles to form magnetic abrasive brush (MAB). The zirconium alloy tube is clamped in the lathe's centre to rotate relative to the MAB, and the distance between the workpiece surface and the magnet is defined as the working gap. Besides, the magnetic field intensity can be controlled by adjusting the working gap.

Figure 2 illustrates the detailed schematic diagram of MAF parts. A couple of Nd–Fe–B permanent magnet poles with high magnetic field intensity are fixed and ranged around the zirconium alloy tube workpiece. Numerous MAPs incur MAB along the magnetic induction line between the workpiece and the magnetic pole. When the workpiece rotates, MAPs are derived by the magnetic force to influence the target surface, and MAF is processed through the abrasive force of MAPs.
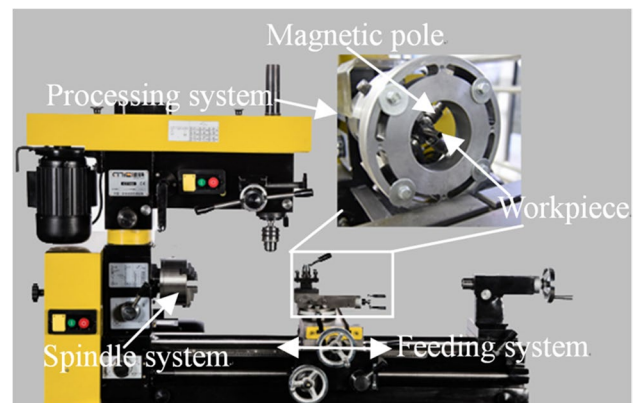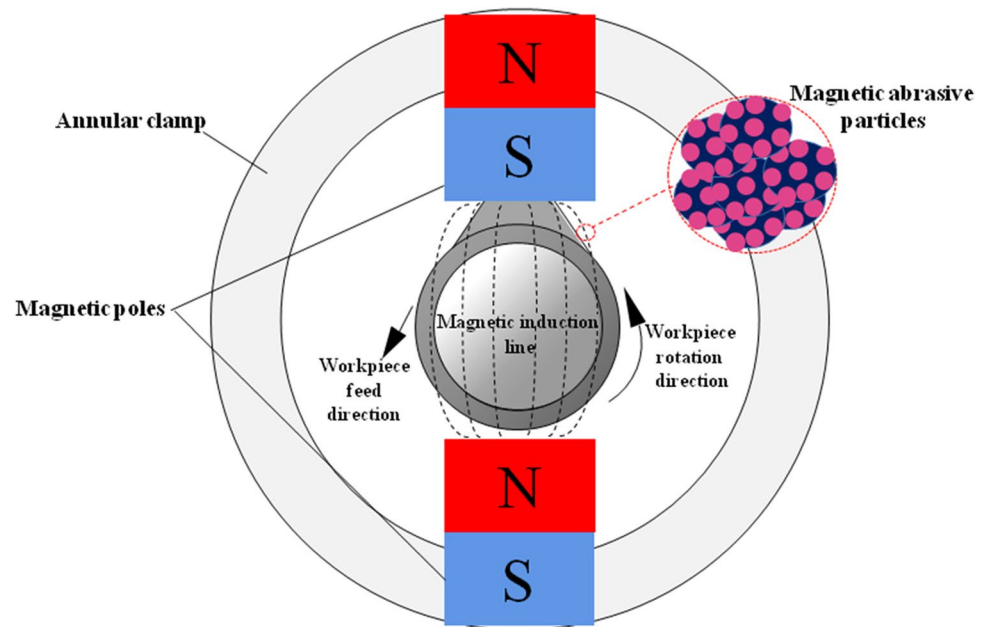

Fig. 1 MAF experimental equipment built by lathe

Fig. 2 Principle schematic diagram of magnetic abrasive finishing for zirconium alloy tube

The normal pressure exerted between a single MAP and the workpiece surface can be calculated as follows [2]:

$$P_n = \frac{B^2}{4u_0} \cdot \frac{3\pi(u_r - 1)\sigma}{3(2 + u_r) + \pi(u_r - 1)\sigma} \tag{1}$$

Here, σ refers to the volume of ferromagnetic phase particles, B is the magnetic field intensity that MAP acts on the workpiece surface, u_0 is the vacuum permeability, while u_r is the magnetic permeability of MAP. Besides, the normal pressure is proportional to magnetic field intensity, MAP susceptibility and MAP volume.

2.2 Optimisation and modelling of the MAF process

During the finishing process, MAB exhibits excellent flexibility and adaptability, and MAPs preferentially squeeze the convex part by the magnetic field force. MAPs also perform a series of operations, such as pressing, scraping and ploughing, during which the tiny bumps on the workpiece surface are removed continuously, leading to a uniform and fine surface. In addition, the efficiency of such MAF process depends on the synergistic effect of the magnetic field and MAP properties.

2.2.1 Optimisation of the magnetic field by changing the magnetic pole shape

Higher processing efficiency and accuracy of the theoretical model require the optimisation of the magnetic field and MAPs because the magnetic field determines the value of

the finishing force, and MAPs contact with the workpiece under the function of the finishing force provided by the external magnetic field. In particular, the normal pressure generated by the magnetic field on MAPs directly affects the indentation depth on the workpiece. Accordingly, varied design of magnetic poles optimises the magnetic field, thus influencing the underlying finishing force for effective MAF processing.

As illustrated in Fig. 3 of the paper, the magnetic pole is constructed from NdFeB, a material with exceptional ferromagnetic properties, of type N38. The pole has a diameter of 20 mm at the base, increasing to 25 mm at the top, and stands 10 mm in height. Centrally located at the top of the pole is a cylindrical recess with a diameter of 5 mm and a depth of 20 mm, designed to facilitate secure attachment to the fixture. In addition, the base of the pole features three slots, each having a width of 3 mm and a depth of 2 mm. These slots accommodate the tumbling of the MAPs, allowing them to roll and self-sharpen. The presence of these slots ensures the uniformity and consistency of the finishing process. Figure 3a displays the simulation results of magnetic poles, which demonstrates the highest magnetic field intensity of magnetic pole at the bottom edge, the scarce effective involvement of MAPs in the MAF process, and the decreased finishing effectiveness and efficiency, resulting in poor surface uniformity and flatness. Figure 3b shows the simulation results of the slotted magnetic pole, which reveals the climbing strength of the magnetic field at the tip of the pole after slotting. As shown in Fig. 4, a straight line was selected when the workpiece was located below the magnetic pole with a working gap of 2 mm, and the magnetic field intensity distribution was simulated. The
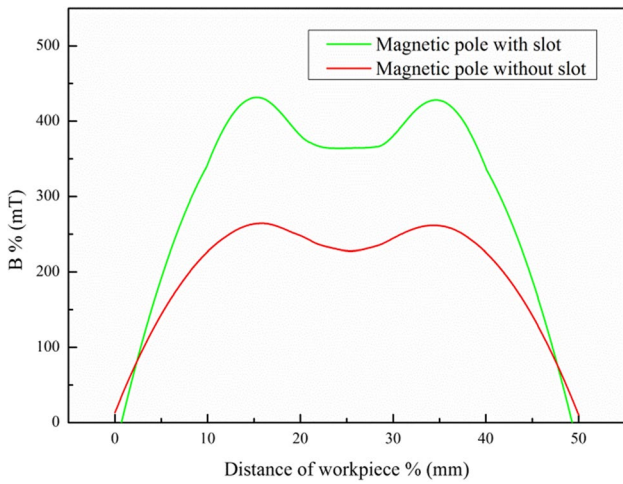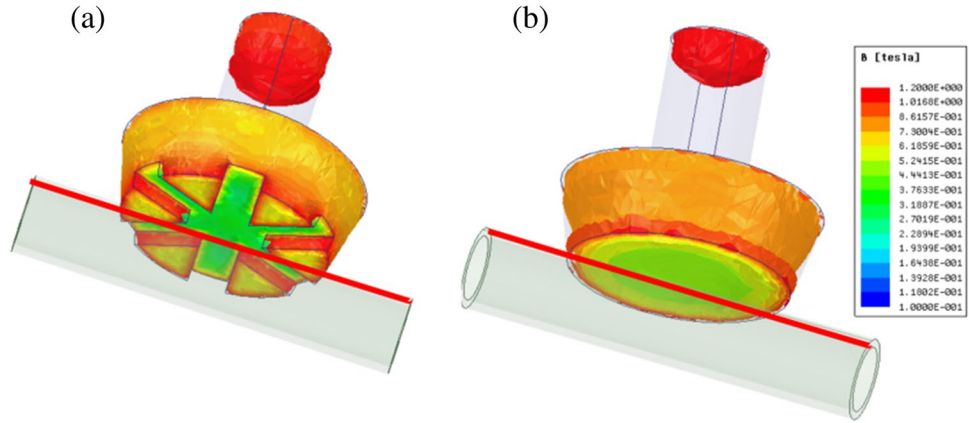
**Fig. 3** Simulation models of magnetic poles

existence of magnetic pole slot provides tumbling space for MAPs, which guarantees the rolling and self-sharpening of MAPs, thus ensuring the uniformity and consistency of finishing.

Figure 5 illustrates the distribution simulation of magnetic field intensity of a circle of zirconium alloy tube surface under two different magnetic poles at the same position with different working gap, which reveals that smaller working gap indicates rising magnetic field intensity. The magnetic field intensity on the zirconium alloy tube's outer surface grows after a magnetic pole is slotted, and the intensity distribution is more uniform, which ensures the efficiency and uniformity during MAF process.

2.2.2 Modelling shell-core MAPs and its preparation

MAPs, as a machining tool, are vital in the MAF process. Based on formula (1), the MAP structure is further optimised following the optimisation of magnetic field to obtain a strong normal pressure and a stable MAF effect. In

Fig. 4 Magnetic field intensity simulation

results show that the magnetic field intensity is significantly increased after the magnetic pole slotting, which enhances the performance and efficiency of MAF process. The

Fig. 5 The magnetic field intensity distribution of a circle on the outer surface of the zirconium alloy tube
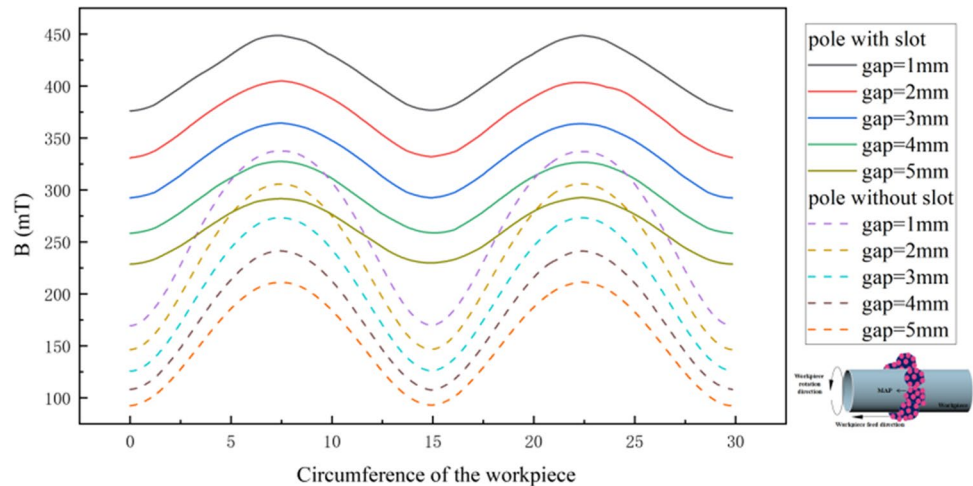
addition to higher permeability, MAP is supposed to have the following features.

1. The microscopic cutting edge of MAPs should be highly wear resistant so that it cannot be destroyed easily.
2. MAPs should exhibit the characteristics of both strong and soft magnetic.
3. MAPs must have a long service life, strong binding force between the hard and ferromagnetic phases, and is difficult to be separated during the MAF process.
4. The abrasive particles only exist on the iron powder's exterior surface, which improves the relative permeability of MAPs, and fully utilises the processing performance of those particles.

This paper prepares MAPs using a two-step mechanical sintering method. Silicon carbide powder (abrasive particles, 10 μm) of 30 vol.% is pre-mixed with iron powder (ferromagnetic particles, 100 μm) in a V-type blender for 30 min, which is then ball milled by high-strength stainless steel balls in a planetary ball mill (QM-3SP04; Nanjing University Instrument Factory) for 10 h at room temperature. As shown in Fig. 6, MAP is obtained by connecting the abrasive particles to the base metal grid with no holding material.

SiC particles uniformly packaged on the ferromagnetic matrix powder are sintered at 1200°C for 2–3 h to ensure they are implanted onto the ferromagnetic matrix's surface after the ferromagnetic matrix powder is molten. Then, the prepared MAPs are annealed to reduce the internal stress between the ferromagnetic matrix and SiC particles, and to reinforce bonding strength. During the sintering process, the surface of the ferromagnetic phase undergoes a molten transformation. Simultaneously, the embedded SiC particles react with the ferromagnetic phase, resulting in the formation of an iron–silicon intermetallic compound. This reaction facilitates the establishment of a metallurgical bond. Subsequently, during the gradual cooling process to room temperature, the internal stresses arising from the disparate thermal expansion coefficients between the ferromagnetic phase and the SiC particles are alleviated. This stress relief mechanism ultimately strengthens the bond between the SiC particles and the ferromagnetic phase [17].

To illustrate the efficacy of the new method, Fig. 7 provides a comparative analysis between MAPs produced using the novel technique and the conventional sintering approach. In particular, Fig. 7b showcases a MAP created via traditional sintering at 1200°C for 2–3 h, utilising 10 μm SiC and 100 μm iron powder. Notably, the resulting MAP exhibits a uniform and highly consistent distribution of cutting edges on the ferromagnetic matrix. This characteristic contributes to the preservation of homogeneity and processing efficiency throughout the cutting process. Compared with the MAP prepared by sintering and crushing, the distribution of SiC particles is avoided in the inside of the ferromagnetic phase.

Figure 8 demonstrates that MAPs prepared by such method exhibit better magnetic characteristics in the same magnetic field compared with standard sintered MAPs. The presence of SiC, a non-magnetic material, has an impact on

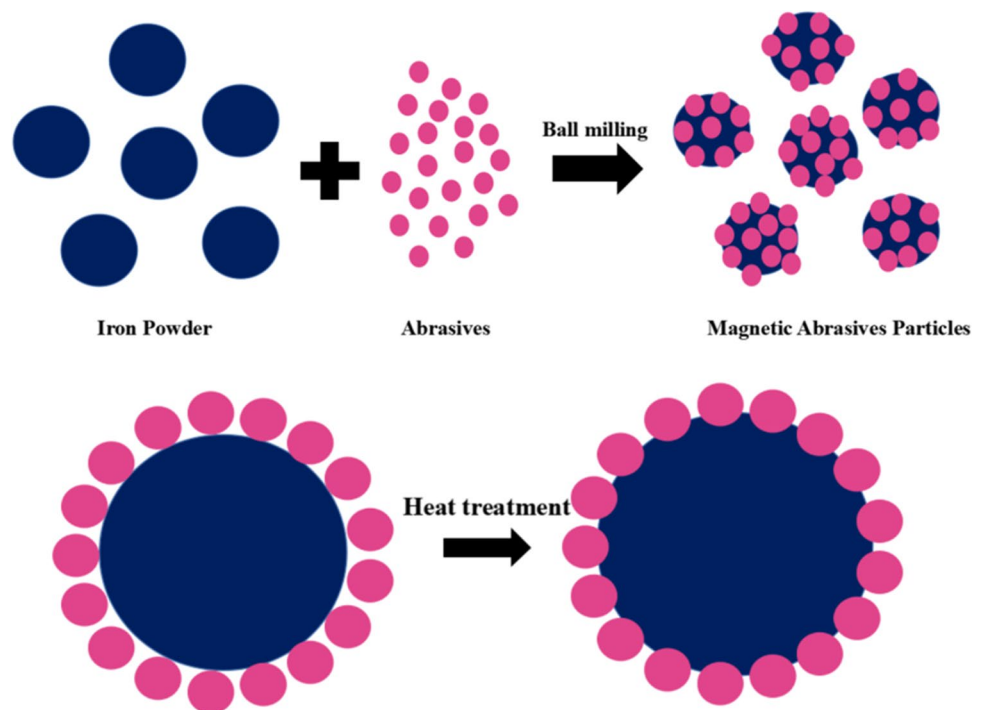Fig. 6 Schematic view of manufacturing of MAP by ball milling

Fig. 7 a The scanning electron microscope of prepared two-step MAPs. **b** The scanning electron microscope of prepared sintered MAPs
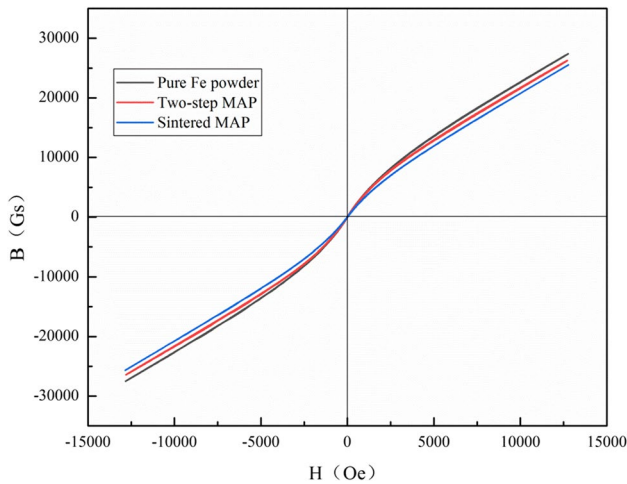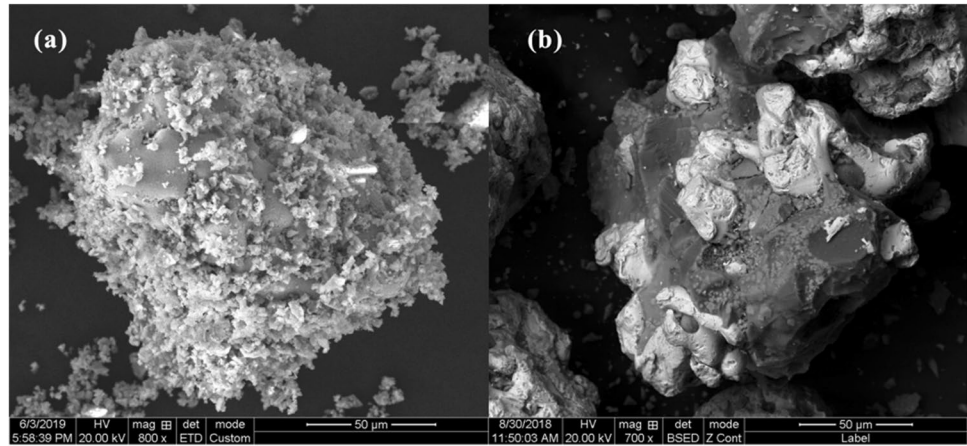

Fig. 8 The B–H curves of the different MAPs

Table 1 Details of constituents of MAP

Material	Weight (g)	Density (g/cm^3)	Volume (cm^3)
Fe	0.75W	7.8	0.75W/7.8
SiC	0.25W	3.21	0.25W/3.21

2.2.3 Estimation of effective abrasive particles and MAP processing force in MAF

MAPs with the ideal theoretical model in Fig. 6 and the real two-step sintered MAPs in Fig. 8 belong to a type of large-size iron particles in the centre with some small-sized SiC particles diffusing around. In order to facilitate the model establishment of the shell-core MAP working process, the iron particles and SiC particles in the prepared MAPs are regarded as spherical shaped, and the size of each MAP is identical. The MAB chains formed by MAPs are continuous, and the flux leakage and flux losses are disregarded. The cross-sectional area of the MAB formed by MAPs equals that of the magnetic pole. The MAP at the bottom of MAB that is in contact with the workpiece is considered to be an active particle. Several SiC particles attached to the MAP produce dents on the zirconium alloy tube under the action of normal force. As shown in Table 1, the mass fraction ratio of iron matrix to silicon carbide is 75 and 25 wt.%, respectively, and the density is 7.8 and 3.21 g/cm^3, respectively. So, the total volume ratio is [19]

$$\sigma = \frac{0.75W/7.8}{0.25W/3.21} = 1.2346 \tag{2}$$

$$\begin{aligned} V_{Fe} &= 4\pi r_{Fe}^3/3 \\ V_{Fe} &= 5.23598 \times 10^{-13} \end{aligned} \tag{3}$$

the magnetic properties of the MAP. In order to address this, a two-step method is employed for the preparation of the MAP, which differs from the conventional sintering method. The two-step method involves initially arranging the SiC particles uniformly on the surface of the iron matrix through ball milling. Subsequently, the morphology of the MAP is preserved during the subsequent sintering and heat treatment stages. This method ensures that the SiC particles are well distributed without damaging the overall structure of the MAP. In contrast, the sintering and crushing method used to prepare the MAP involves sintering the ferromagnetic phase with SiC in a random combination, followed by crushing the resulting material. This process leads to the entrapment and accumulation of SiC particles within the ferromagnetic phase. As a result, the proportion of the ferromagnetic phase within the MAP decreases, ultimately leading to a reduction in its saturation magnetisation intensity [18].

$$V_{SiC} = 4\pi r_{SiC}^3 / 3$$
$$V_{SiC} = 5.23598 \times 10^{-16} \tag{4}$$

$$N = V_{Fe}/V_{SiC} \times \frac{0.75W/7.8}{0.25W/3.21} = 115.87 \tag{5}$$

On a single MAP, the ratio of SiC to iron particles is 115.87. As a result, the spherical surface of an iron particle is expected to be uniformly surrounded by 115–116 SiC particles.

The number of active particles is defined to calculate the total removal. The SiC particles are visibly arranged on a single MAP, and evenly distributed on the surface of Fe powders. When processing begins, the three abrasive particles contact the workpiece simultaneously. After being pressed into a certain depth, the surrounding SiC particles contact the workpiece again. Figure 9 demonstrates the same processing height of SiC particles No. 1, 2 and 3. When the depth of SiC particles pressed into the workpiece is greater than Δh, SiC particles No. 4, 5 and 6 start to contact the workpiece. According to the geometric relationship between particles No. 1, 2, 3 and No. 4, 5, 6, the height difference

of contacts is obtained. Given the geometric relation, SiC particles are pressed into the workpiece, so three SiC particles involve in processing for each MAP.

In MAF process, several SiC particles on the layer of active particles are indented in the workpiece under normal force. Figure 10 illustrates the finishing force acting on active abrasive particles.

The normal pressure applied to a single MAP that is transmitted to the three SiC particles results in indentations on the workpiece surface. The normal force of a single MAP is calculated using the formula

$$F_n = P_n \bullet \frac{3\pi D_{abr}^2}{4} \tag{6}$$

where D_{abr} is the diameter of SiC particle.

MAF essentially removes material from the workpiece surface through numerous tiny abrasive particles. The abrasive particles on MAPs contact the workpiece surface under the force provided by the magnetic field. The contact between the workpiece and MAB is complex, including coupling multiple actions such as squeezing, scratching, ploughing and cutting. MAF process is divided into two stages

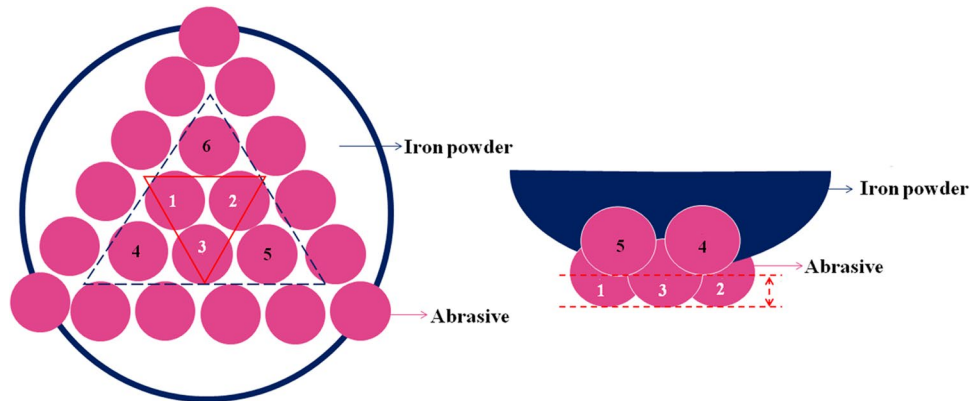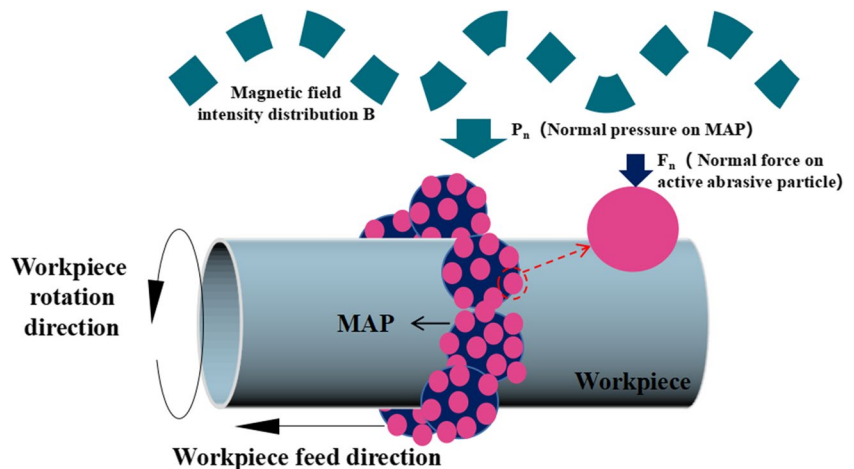Fig. 9 The calculation schematic of active abrasives

Fig. 10 Schematic view of cylindrical tube magnetic abrasive finishing

based on the deformation behaviour of the material, elastic deformation and plastic deformation. The transition between the two is determined by the cut depth made by the abrasive particles in the workpiece. Therefore, the staged action process of a single abrasive particle can be analysed according to the deformation form. In order to mathematically simplify the problem, it is assumed that the characteristics of the workpiece are not modified due to less material removal during the MAF process.

In the elastic deformation stage, the average pressure acting on a single abrasive particle can be calculated based on the elastic mechanics theory [20]:

$$P_{abr} = \frac{1}{n}\left(\frac{16E_cF_n}{9R^2}\right)^{\frac{1}{3}} \tag{7}$$

$$\delta_E = \left(\frac{9F_n^2}{16RE_c^2}\right)^{\frac{1}{3}} \tag{8}$$

where P_{abr} stands for the average pressure of abrasive particles, δ_E the elastic cutting depth, E_c the contact elastic modulus of abrasive particles and workpiece, the elastic modulus of the workpiece, E_k the elastic modulus of the abrasive particles, while v_i and v_k are the Poisson ratio of workpiece and the abrasive particles, respectively. Besides, the spherical radius is R when the applied force is F_n.

$$\frac{1}{E_c} = \frac{1-v_k^2}{E_k} + \frac{1-v_i^2}{E_i} \tag{9}$$

The Brinell hardness of the workpiece surface is set as HB. According to the elastoplastic deformation theory, plastic deformation will occur when the average pressure of the workpiece $P_{abr} \geq$ HB/3, and the workpiece only undergoes elastic deformation when $P_{abr} <$ HB/3. In addition, the maximum penetration depth of abrasive particles in the latter situation is obtained [21]:

$$\delta_{E_{max}} = \frac{\pi R H_B^2}{16E_c^2} \tag{10}$$

For the zirconium alloy tube, $E_i = 0.9$ GPa and $\nu_i = 0.14$. For SiC ceramics, $E_k = 420$ GPa and $\nu_k = 0.14$. The value of δ_{Emax} is 2.3×10^{-4} μm.

In plastic deformation stage, the workpiece will undergo plastic deformation when the depth of abrasive particles exceeds δ_{Emax}, which incurs material removal. A certain degree of elastic deformation can also be observed. The elastic deformation in this process is calculated as follows:

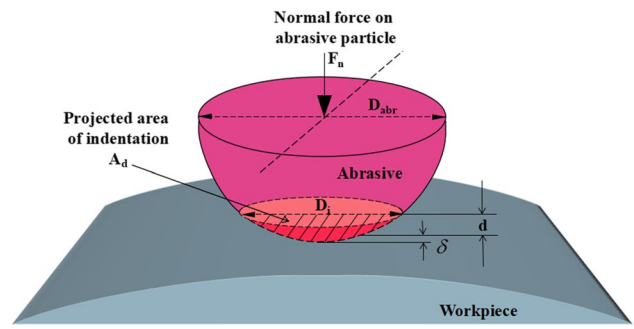$$\delta_P = \left(\frac{0.6\pi H_B}{2E_c}\right)^2 R \tag{11}$$

Fig. 11 Schematic view of single abrasive particle acted on workpiece

When the depth of abrasive particles exceeds δ_P, the workpiece will experience plastic deformation, which leads to material removal. The Brinell hardness number (H_{BHN}) is proportional to the indentation depth as below [22]:

$$H_{BHN} = \frac{2F_n}{\pi D_{abr}\left(D_{abr} - \sqrt{D_{abr}^2 - D_i^2}\right)} \tag{12}$$

Based on the geometric relationship shown in Fig. 11, the indentation depth of an abrasive particle is obtained:

$$d = \frac{D_{abr}}{2} - \frac{1}{2}\sqrt{D_{abr}^2 - D_i^2} - \left(\delta_{E_{max}} + \delta_P\right) \tag{13}$$

2.2.4 Modelling of surface roughness Ra

The reduction of surface roughness in MAF process comes down to the interaction between MAPs and the workpiece, and the final roughness accuracy of MAF process depends on the quality of MAPs and the poles. Therefore, surface roughness serves as an index of the finishing capacity of MAPs. In order to quantitatively describe the capacity of the new MAPs, this paper theoretically explores surface roughness modelling, which promotes a thorough understanding of MAF process.

The groove generated by the indented abrasive particle's projected area A_d is expressed as [23]

$$A_d = \frac{D_{abr}^2}{4}\sin^{-1}\frac{2\sqrt{d(D_{abr}-d)}}{D_{abr}} - \sqrt{d(D_{abr}-d)}\left(\frac{D_{abr}}{2} - d\right) \tag{14}$$

The length of abrasive coverage is l_w, and the number of abrasive particles effectively participating in the process is calculated as follows:

Fig. 12 The shape of roughness peaks
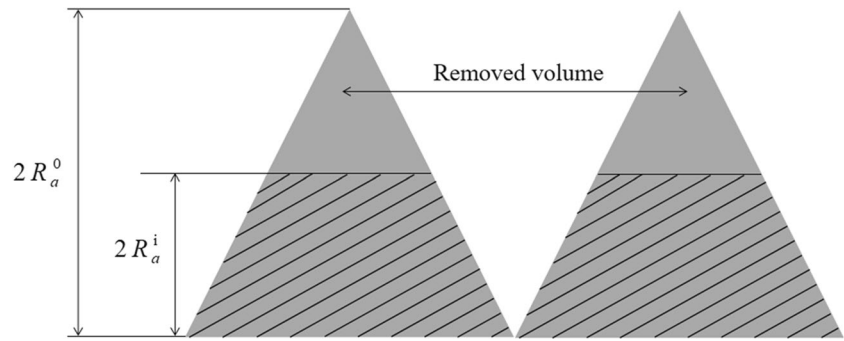
$$n = \delta \times \frac{l_w}{D_{map}} \tag{15}$$

From the geometry of Fig. 12 the removed volume is obtained as follows [24]:

$$V = \frac{(R_a^0 - R_a^i)^2}{R_a^0} l_w^2 \tag{16}$$

The final roughness can be expressed as follows:

$$R_a^i = R_a^0 - \frac{n \times A_d}{l_w} \tag{17}$$

Each experiment adopts a 1-m zirconium alloy tube sample, and the finishing time T_f of one pass is determined according to the feed speed v_f.

$$T_f = 1\text{m}/v_f \tag{18}$$

The roughness that results from one MAF pass is expressed as

$$Ra = 3nV_R R_a^i Tf \tag{19}$$

In the simultaneous processing of three SiC particles on a MAP, several parameters come into play. Let us define the relevant variables:

- V_R represents the rotation speed of the workpiece;
- n signifies the number of abrasive particles effectively engaged in MAF process;
- R_a^i denotes the roughness change resulting from a single rotation;
- T_f represents the processing time required for one pass.

As shown in Fig. 2, the MAF experiment is carried out on a lathe with a magnetic pole after slotting. The effect of processing parameters on processing force is investigated using a single-factor experiment. The contrast experiment is also conducted to explore the relationship between several process factors. The experiment mainly aims to verify the reliability of the prediction model.

3 Discussion on experimental verification of mathematical modelling results

In order to validate the aforementioned model and deepen the understanding of the relationship between material removal and surface roughness reduction, the experimental observations are compared with the predicted theoretical conclusions from formula (16). The experimental results were measured by TR200 roughness measuring instrument. The sample length was 1.5 mm, and 15 points were randomly measured. The average value was taken as the measurement result. Each group of experiments was repeated three times. As displayed in Table 2, single-factor analysis was employed to design the experiments. In this study, key factors affecting the actual MAF process are selected. The effect of working gap, rotational speed and processing pass on MAF process is also investigated. Besides, finishing experiments are performed on a zirconium alloy tube. The formula below is taken to calculate the percentage change %ΔRa:

Table 2 The parameters in the MAF process

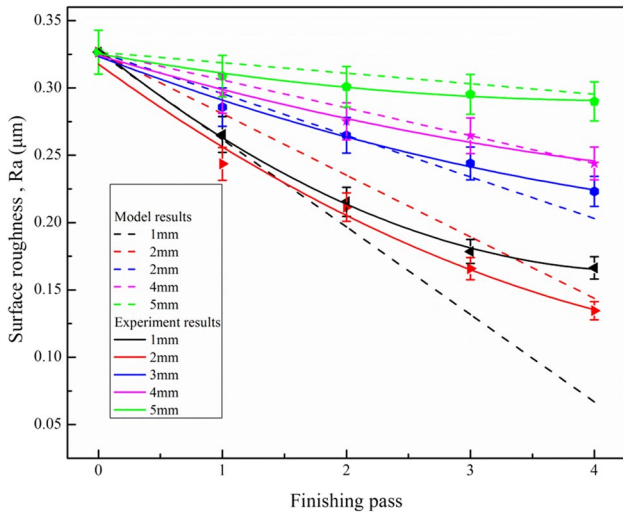| Items	Conditions
Workpiece	Zirconium alloy tube (length: 1.5 m, diameter: 10 mm)
Magnetic pole	N38 NdFeB
Magnetic abrasive particle	Fe+SiC boundtype
Feed speed	168 mm/min
Finishing time	1–5 pass
Gap between magnet and workpiece (mm)	1, 2, 3, 4, 5
Workpiece's rotational speed (rpm)	600, 800, 1000, 1600

Fig. 13 Effect of working gap on surface roughness

Fig. 14 Effect of rotation speed on surface roughness

$$\%\Delta Ra = \frac{\left(Ra_{beforeMAF} - Ra_{afterMAF}\right)}{Ra_{beforeMAF}} \quad (20)$$

3.1 Effect of the working gap between magnetic poles and workpiece

Working gap, as the most critical process parameter, directly influences the driving force of MAP. In this study, the working gap is defined as the distance between the magnetic pole and the outer wall of the workpiece tube. Its role on $\%\Delta Ra$ is explored by simulation and experiment with MAF. Figure 5 depicts the magnetic field intensity distribution of working gap simulation at 1, 2, 3, 4 and 5 mm. Figure 13 demonstrates that the roughness decreases with larger working gap in both simulation and experimental curves, which highlights that as the working gap enlarges, the effect of magnetic field intensity on MAPs weakens. According to the theoretical analysis of formula (1), the removal of material directly depends on the indentation depth of SiC particles. Formulas (2) and (3) reveal that the indentation depth is determined by the magnetic field intensity in the working gaps. As a result, the smaller the working gap, the greater the magnetic field intensity on workpiece surface, and thus the greater the force driving the MAP processing. The peaks of original burrs and surface defects are easier to remove to obtain favourable roughness completely. Instead, the magnetic field intensity decreases as the working gap rises, resulting in a decline in indentation force and depth. Besides, incomplete peak removal results in a rough surface. Therefore, it can be seen from the predicted trend curve that $\%\Delta Ra$ decreases as the working gap increases.
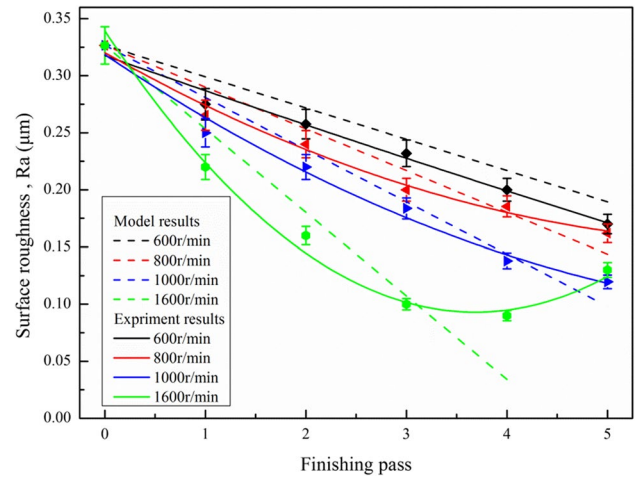
In the experiment, the trend of the measured value is consistent with the predicted value. When the working gap is reduced to 1 mm, $\%\Delta Ra$ shows a downward trend. This is because in a larger working gap, MAB lacks flexibility, and MAPs acting on the workpiece surface cannot be freely rolled to achieve self-sharpening, which reduces the processing efficiency of MAF. After the used MAPs are worn, the fresh MAPs cannot replace the used in processing, resulting in a lower material removal rate and better surface quality. Nonetheless, as the working gap increases, the magnetic field intensity decreases, leading to a smaller force driving the MAP processing. Therefore, the combination of the two effects incurs an optimum value of $\%\Delta Ra$. Figure 13 reveals that an optimal value of Ra in surface roughness exists near the 2-mm working gap at a certain speed. When the working gap is 1 mm, 2 mm, 3 mm, 4 mm and 5 mm, the $\%\Delta Ra$ is 49.06%, 58.79%, 31.68%, 25.33% and 11.21%, respectively, and the final roughness is 0.166 μm, 0.134 μm, 0.223 μm, 0.244 μm and 0.29 μm, respectively. When the working gap is 2 mm, the $\%\Delta Ra$ and the final Ra peak.

3.2 Effect of workpiece's rotational speed under the magnetic field acting on the MAPs

The rotation speed of workpiece is another important factor influencing the efficiency and quality of MAF process, which determines the frequency of MAPs acting on the workpiece per unit time. Accordingly, the working gap is 2.0 mm, the MAP size is 110 μm and the effect of processing at four workpieces' rotation speed is considered.

Figure 14 illustrates the improvement in $\%\Delta Ra$ with higher rotation speed in simulation and experiment curves, which is because higher rotation speed leads to more turns of MAPs around the workpiece simultaneously and more

MAPs acting on the workpiece surface simultaneously. As shown in Fig. 14, the difference between simulation results and experimental results increases significantly with higher rotation speed. The variation of %ΔRa in simulation results is more obvious than that of experimental results, which comes down to that the workpiece becomes unstable when the rotation speed reaches a certain level during the experiment, resulting in an uneven processing effect. Simultaneously, accelerated wear occurs, and MAPs blunt faster and require more frequent replacement. Given the fixed replacement time, MAF performance will wane when the circumferential velocity of the workpiece exceeds a certain value. $\Delta Ra\%$ is 47.95%, 50.39%, 63.38% and 60.19% at 600 r/min, 800 r/min, 1000 r/min and 1600 r/min, and the final roughness is 0.170 μm, 0.162 μm, 0.119 μm and 0.131 μm. %ΔRa and final roughness peak at 1000 r/min.

3.3 Effect of processing passes on material removal mechanism of workpiece

Apart from the working gap and rotation speed, processing passes determine the MAF accuracy. Figure 15 shows the effect of processing passes on surface roughness during MAF process. When all other parameters are held constant, surface roughness decreases with more processing passes, which comes down to the extended processing time for MAPs involved in the MAF process.

Figure 15 demonstrates the rapid decline of surface roughness in the initial processing stage, the parabolical climbing material removal rate and the high processing efficiency. As processing passes increase, the decreasing trend of surface roughness weakens until it becomes saturated, which is mainly due to the relatively rough surface of the workpiece at the beginning of MAF process. Due to sharp point effect, the magnetic lines of force are dense at
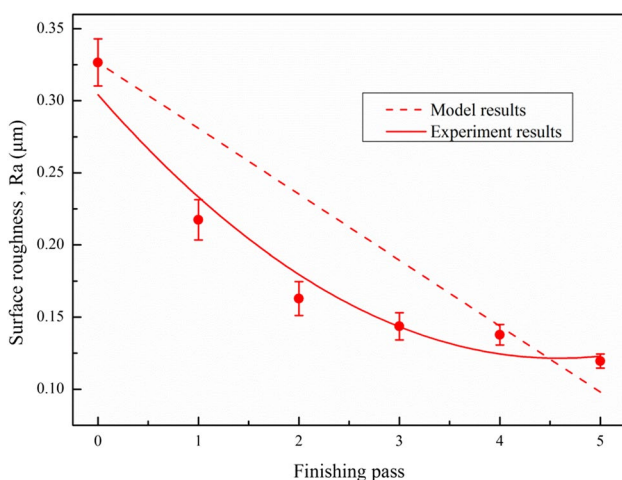
the microscopic protrusions or sharp points of the workpiece, and the MAF pressure generated is immense. The MAPs quickly grind away the protrusions. As the number of processing passes increases, the workpiece's surface roughness decreases, so does the processing efficiency. In MAF process, if the contact stresses combined exceeds a critical value, the irregularities on the material surface will be removed. The greater the roughness, the easier the material will be removed. When the surface roughness value is reduced, the apparent contact area between the MAPs and the workpiece expands, thus reducing the contact stress. Once the contact stress drops below the critical level, the irregular shear is difficult to stabilise.

Peaks on the tube are easily sheared off during the early phase of MAF, eliminating a wide range of surface roughness and material mass by the first pass. The polishing efficiency decreases with time as the tube revolution increases because more materials must be removed to reduce the surface roughness compared with the previous MAF process.

3.4 Comparison and analysis of surface morphology for high-precision MAF behaviours

The verification studies conducted indicate that the actual evolution of roughness closely aligns with the predicted results, albeit with slight deviations. These deviations can be attributed to the fact that the roughness model developed in this study is based on the material removal mechanism of an ideal theoretical model, considering a single MAP. The model predicts a linear relationship between roughness and processing time and frequency. However, the actual MAF process involves a range of complex factors, including extrusion, friction, collision and tumbling, among others. These additional complexities introduce variations and intricacies not accounted for in the simplified theoretical model. Specifically, certain process conditions such as a working gap of 1 mm and a workpiece rotation speed of 1600 r/min exacerbate the degradation of MAPs, resulting in increased disparities between the experimental observations and the theoretical predictions.

The sample surface is observed with an atomic force microscope to investigate the removal mechanism of MAF process. Figure 16a describes the surface roughness before finishing, which reveals the obvious defects on the surface before MAF process. Figure 16b illustrates the 2.0-mm working gap and 1000-rpm workpiece rotation speed after five passes, which demonstrates the uniform and fine microscopic surface, the removal of defects and the obvious better surface quality after the MAF process.

Fig. 15 Effect of finishing pass on surface roughness

Fig. 16 **a** Surface roughness profiles before finishing. **b** Surface roughness profiles after finishing
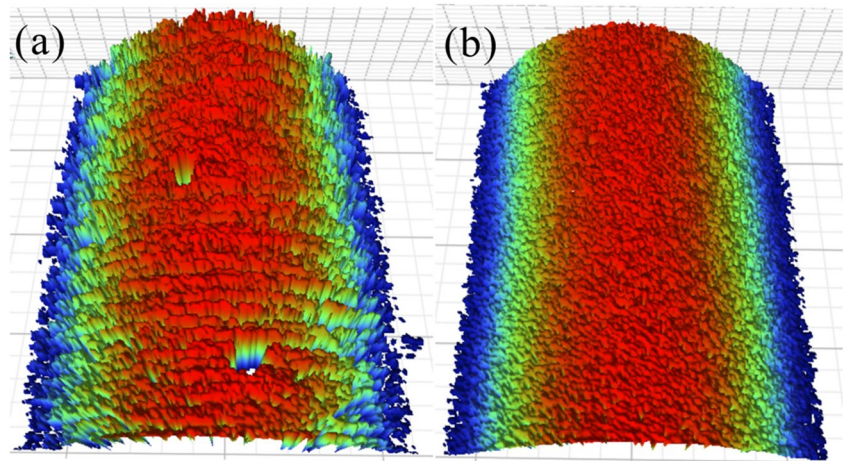
4 Conclusions

In order to achieve magnetic abrasive finishing featuring high efficiency and precision, this paper optimises the magnetic field distribution around the tube's outer surface and establishes a surface roughness model of the MAF process, which takes into account elastic deformation effect, and the association between material removal mechanism and surface roughness. According to the simulation and experimental results, the following conclusions are drawn:

1. The magnetic field intensity is closely related to the shape of the magnetic pole. The maximum magnetic field formed on the tube surface through the slotted magnetic pole rises from 0.36 to 0.49 T, and the distribution is more uniform, which effectively guarantees the processing efficiency of the tubular workpiece.
2. The MAP prepared by the two-step method of ball milling and sintering has higher magnetic permeability, and the abrasive particles are evenly distributed on the MAP surface. The three active abrasive particles contact the workpiece at the same time. The surface roughness model in the MAF process is further established by the indentation force on the active abrasive particles and the material removal.
3. The working gaps between magnetic poles and the tube outer surface, and the rotation speed between the MAPs and the tube well are crucial for MAF efficiency and precision. The working gap of 2 mm and the rotation speed of 1000 r/min are optimised based on real experiments.

Declarations

Conflict of interest The authors declare no competing interests.

References

1. Platt P, Allen V, Fenwick M, Gass M, Preuss M (2015) Observation of the effect of surface roughness on the oxidation of Zircaloy-4. Corrosion Sci 98:1–5. https://doi.org/10.1016/j.corsci.2015.05.013
2. Shinmura T, Takazawa K, Hatano E, Matsunaga M, Matsuo T (1990) Study on magnetic abrasive finishing. CIRP Annals 39:325–328. https://doi.org/10.1016/S0007-8506(07)61064-6
3. Yamaguchi H, Shinmura T, Ikeda R (2007) Study of internal finishing of austenitic stainless steel capillary tubes by magnetic abrasive finishing. J Manuf Sci Eng 129:885–892. https://doi.org/10.1115/1.2738957
4. Yamaguchi H, Kang J, Hashimoto F (2011) Metastable austenitic stainless steel tool for magnetic abrasive finishing. CIRP Annals 60:339–342. https://doi.org/10.1016/j.cirp.2011.03.119
5. Wang C, Cheung CF, Ho LT, Yung KL, Kong LB (2019) A novel magnetic field-assisted mass polishing of freeform surfaces. J Mater Process Technol 279:116552. https://doi.org/10.1016/j.jmatprotec.2019.116552
6. Zhou K, Chen Y, Du ZW, Niu FL (2015) Surface integrity of titanium part by ultrasonic magnetic abrasive finishing. Int J Adv Manuf Technol 80:997–1005. https://doi.org/10.1007/s00170-015-7028-z
7. Kwak J-S (2009) Enhanced magnetic abrasive polishing of non-ferrous metals utilizing a permanent magnet. Int J Mach Tools Manuf 49:613–618. https://doi.org/10.1016/j.ijmachtools.2009.01.013

8. Li W, Li X, Yang S, Li W (2018) A newly developed media for magnetic abrasive finishing process: material removal behavior and finishing performance. J Mater Process Technol 260:20–29. https://doi.org/10.1016/j.jmatprotec.2018.05.007

9. Kala P, Sharma V, Pandey PM (2017) Surface roughness modelling for double disk magnetic abrasive finishing process. J Manuf Process 25:37–48. https://doi.org/10.1016/j.jmapro.2016.10.007

10. Misra AM, Pandey P, Dixit US (2017) Modeling of material removal in ultrasonic assisted magnetic abrasive finishing process. Int J Mech Sci 131–132:853–867. https://doi.org/10.1016/j.ijmecsci.2017.07.023

11. Jain VK, Saren KK, Raghuram V, Sankar MR (2019) Force analysis of magnetic abrasive nano-finishing of magnetic and non-magnetic materials. Int J Adv Manuf Technol 100:1137–1147. https://doi.org/10.1007/s00170-016-8954-0

12. Jayswal SC, Jain VK, Dixit PM (2005) Modeling and simulation of magnetic abrasive finishing process. Int J Adv Manuf Technol 26:477–490. https://doi.org/10.1007/s00170-004-2180-x

13. Jain VK (2009) Magnetic field assisted abrasive based micro-/nano-finishing. J Mater Process Technol 209:6022–6038. https://doi.org/10.1016/j.jmatprotec.2009.08.015

14. Jain VK, Jayswal SC, Dixit PM (2007) Modeling and –. Mater Manuf Process 22:256–270 https://doi.org/10.1080/10426910601134096

15. Misra A, Pandey PM, Dixit US (2017) Modeling and simulation of surface roughness in ultrasonic assisted magnetic abrasive finishing process. Int J Mech Sci 133:344–356. https://doi.org/10.1016/j.ijmecsci.2017.08.056

16. Gao YW, Zhao YG, Zhang GX, Yin FS, Zhang HY (2020) Modeling of material removal in magnetic abrasive finishing process with spherical magnetic abrasive powder. Int J Mech Sci 177:105601. https://doi.org/10.1016/j.ijmecsci.2020.105601

17. Zhang GX, Zhao YG, Zhao DB, Zuo DW, Yin FS (2013) New iron-based SiC spherical composite magnetic abrasive for magnetic abrasive finishing. Chin J Mech Eng 26:377–383. https://doi.org/10.3901/CJME.2013.02.377

18. Luo ZG, Fan XA, Feng B, Yang ZJ, Chen DY, Jiang SW, Wang J, Wu ZY, Liu X, Li GQ, Li YW (2021) Highly enhancing electromagnetic properties in Fe-Si/MnO-SiO$_2$ soft magnetic composites by improving coating uniformity. Adv Powder Technol 32:4846–4856. https://doi.org/10.1016/j.apt.2021.10.039

19. Shukla VC, Pandey PM, Dixit US, Roy A, Silberschmidt V (2017) Modeling of normal force and finishing torque considering shearing and ploughing effects in ultrasonic assisted magnetic abrasive finishing process with sintered magnetic abrasive powder. Wear 390–391:11–22. https://doi.org/10.1016/j.wear.2017.06.017

20. Jourani A, Hagège B, Bouvier S, Bigerelle M, Zahouani H (2013) Influence of abrasive grain geometry on friction coefficient and wear rate in belt finishing. Tribol Int 59:30–37. https://doi.org/10.1016/j.triboint.2012.07.001

21. Qi J, Zhang D, Li S, Chen B (2016) A micro-model of the material removal depth for the polishing process. Int J Adv Manuf Technol 86:2759–2770. https://doi.org/10.1007/s00170-016-8385-y

22. Alam Z, Jha S (2017) Modeling of surface roughness in ball end magnetorheological finishing (BEMRF) process. Wear 374–375:54–62. https://doi.org/10.1016/j.wear.2016.11.039

23. Stradling AW (1993) The physics of open-gradient dry magnetic separation. Int J Mineral Process 39:1–18. https://doi.org/10.1016/0301-7516(93)90048-F

24. Jain RK, Jain VK, Dixit PM (1999) Modeling of material removal and surface roughness in abrasive flow machining process. Int J Mach Tools Manuf 39:1903–1923. https://doi.org/10.1016/S0890-6955(99)00038-3